









RESEARCH ARTICLE | AUGUST 12 2024

# 2D core ion temperature and impurity density measurements with Coherence Imaging Charge Exchange Recombination Spectroscopy (CICERS) at Wendelstein 7-X (invited)

Special Collection: [Proceedings of the 25th Topical Conference on High-Temperature Plasma Diagnostics](#)

R. Lopez-Cansino ; V. Perseo ; E. Viezzer; O. P. Ford ; M. Kriete ; T. Romba ; J. Rueda-Rueda ; P. Z. Poloskei ; F. Reimold ; W7-X Team


 Check for updates


Rev. Sci. Instrum. 95, 083524 (2024)


<https://doi.org/10.1063/5.0219483>


  
View Online


  
Export Citation

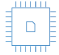
  
Nanotechnology & Materials Science


  
Optics & Photonics

  
Impedance Analysis

  
Scanning Probe Microscopy

  
Sensors


  
Failure Analysis & Semiconductors



Unlock the Full Spectrum.  
From DC to 8.5 GHz.

Your Application. Measured.

Find out more



# 2D core ion temperature and impurity density measurements with Coherence Imaging Charge Exchange Recombination Spectroscopy (CICERS) at Wendelstein 7-X (invited)

Cite as: Rev. Sci. Instrum. 95, 083524 (2024); doi: 10.1063/5.0219483

Submitted: 17 May 2024 • Accepted: 14 July 2024 •

Published Online: 12 August 2024



View Online



Export Citation



CrossMark

R. Lopez-Cansino,<sup>1,a)</sup> V. Perseo,<sup>2</sup> E. Viezzer,<sup>1</sup> O. P. Ford,<sup>2</sup> M. Kriete,<sup>3</sup> T. Romba,<sup>2</sup>  
J. Rueda-Rueda,<sup>1</sup> P. Z. Poloskei,<sup>2</sup> F. Reimold,<sup>2</sup> and W7-X Team<sup>b)</sup>

## AFFILIATIONS

<sup>1</sup>Department of Atomic, Molecular and Nuclear Physics, University of Seville, Seville, Spain

<sup>2</sup>Max-Planck-Institut für Plasmaphysik, Greifswald, Germany

<sup>3</sup>Auburn University, Auburn, Alabama 36849, USA

**Note:** This paper is part of the Special Topic on Proceedings of the 25th Topical Conference on High-Temperature Plasma Diagnostics.

<sup>a)</sup>Author to whom correspondence should be addressed: rlopez1@us.es

<sup>b)</sup>See Pedersen *et al.* 2022 for the W7-X Team.

## ABSTRACT

Coherence Imaging Charge Exchange Recombination Spectroscopy (CICERS) is an imaging diagnostic installed in Wendelstein 7-X from which 2D maps of ion temperature ( $T_i$ ) and impurity density ( $n_Z$ ) are obtained. The improved spatial resolution and coverage, as compared to standard Charge eXchange Recombination Spectroscopy (CXRS), with which these parameters can be assessed, come at the expense of spectral resolution, requiring the development of new strategies to isolate the active charge exchange contribution from passive and Bremsstrahlung radiation. In this work, a new approach based on the modeling of background radiation is presented and applied to the derivation of 2D  $T_i$  maps. These are compared to the  $T_i$  profiles derived from standard CXRS, which found excellent agreement up to the edge ( $\rho > 0.8$ ). The CICERS view is implemented in the pyFIDAsim code, which is used to provide further insight into the spatial localization of the radiation as measured by the diagnostic. Moreover, an absolute intensity calibration is carried out, and, coupled with pyFIDAsim, the first 2D  $n_C$  maps are obtained and validated against CXRS data.

Published under an exclusive license by AIP Publishing. <https://doi.org/10.1063/5.0219483>

## I. INTRODUCTION

Coherence Imaging Spectroscopy (CIS) is a state-of-the-art imaging and plasma diagnostic technique based on polarization interferometry. Its working principle consists of the generation of a 2D interference pattern via birefringent crystals from which 2D maps of relevant plasma parameters such as ion temperature ( $T_i$ ), impurity density ( $n_Z$ ), or flow velocities ( $v_Z$ ) can be derived. As an example, this technique has been used to measure flows in the Scrape-Off Layer (SOL) of Wendelstein 7-X plasmas from CIII radiation.<sup>1</sup> In the spatial heterodyne configuration,<sup>2</sup> the crystal(s) are arranged such that the resulting interference pattern consists of a set of parallel fringes. The diagnostic signal can be interpreted as

$$S(x, y) = \frac{I_0(x, y)}{2} [1 + \zeta(x, y) \cos \Phi(x, y)], \quad (1)$$

where  $I_0$  is the intensity of the measured radiation,  $\zeta$  is the contrast of the fringe pattern, and  $\Phi$  is the phase shift introduced by the birefringent plates. Here,  $(x, y)$  refer to different pixel positions of the sensor where the fringe pattern is recorded.  $I_0$ ,  $\zeta$ , and  $\Phi$  are known as the interferogram parameters, which can be recovered from the raw signal by the use of the 2DFFT.<sup>3</sup> In that sense, the only experimental information provided by the diagnostic itself is these three parameters, which encode the spectral line shape of the collected radiation. The lack of spectral resolution to discriminate between different radiation components limits the CIS technique to

simple or well-known spectra. For that reason, typical CIS diagnostics include a narrow bandpass filter centered on the emission line under study. An attempt to use the spatial heterodyne CIS technique to infer ion temperatures in the SOL demonstrated the limitations of the technique for this purpose, as for such temperatures ( $\sim 20$  eV), the Doppler broadening mechanism is comparable to the Zeeman splitting broadening,<sup>4</sup> and the spectral information is not sufficient to separate the effects. For that matter, the multi-delay CIS system has recently been developed.<sup>5</sup>

Unlike most CIS systems, which are used for measurements of the Scrape-Off Layer (SOL), the CICERS<sup>6</sup> (Coherence Imaging Charge Exchange Recombination Spectroscopy) diagnostic performs measurements of radiation in the core of Wendelstein 7-X (W7-X) plasmas. It is focused and optimized to measure Charge eXchange (CX) radiation, which is generated after neutral beam injection (NBI) injected neutrals undergo a CX reaction with an ion species present in the plasma and can be used to infer 2D maps of the same plasma parameters as with standard CXRS. The availability of these maps is inherently interesting because of the enhanced spatial resolution with which these parameters can be determined. In addition, having a toroidal view, it can directly image a large part of the poloidal cross section of the plasma, enabling it to identify 2D structures in the profiles, which, e.g., can be used to assess the effect of core magnetic islands on these profiles.<sup>7</sup>

An overview of the CICERS diagnostic is introduced in Sec. II, where the limitations of the diagnostic due to the presence of background radiation are addressed. A new approach to deal with background radiation based on the modeling of the different sources is shown in Sec. III. In Sec. IV, the implementation of CICERS in the pyFIDASim code is introduced and used to further characterize the spatial localization of the active CX radiation, and finally, in Sec. V, the code is used to derive an experimental 2D impurity density map.

## II. COHERENCE IMAGING CHARGE EXCHANGE RECOMBINATION SPECTROSCOPY

CICERS<sup>6</sup> employs the spatial heterodyne single delay approach,<sup>2</sup> and its crystals are optimized for the high temperatures present in the core of W7-X plasmas ( $T_i \sim 2$  keV). It uses an  $\alpha$ -BBO 2.5 mm delay plate and two  $\alpha$ -BBO 10 mm displacer plates set up as a Savart plate.<sup>6</sup> CICERS was installed in the W7-X OP2.1 experimental campaign, during which a narrow bandpass filter (full width half maximum  $\sim 2$  nm) centered around the CVI ( $C^{5+}$ ,  $n = 8 \rightarrow n = 7$ ,  $\lambda = 529.05$  nm) CX emission line was used. All the results presented here are focused on this impurity species and emission line. More information on the set-up and calibration procedure used for the diagnostic can be found in Ref. 6.

The CIS technique provides limited information about the spectral content of the measured radiation, so it is helpful to have a proper understanding of the behavior of the CX radiation. The radiation is well-localized along each diagnostic Line Of Sight (LOS), with a narrow emissivity distribution around the neutral beam function along each.<sup>8,9</sup> This is confirmed by the implementation of the CICERS view in the pyFIDASim code (see Sec. IV for details). The high temperatures present in the core of W7-X plasmas make the Doppler effect the dominant broadening mechanism, and the Zeeman splitting becomes a minor correction factor for which the

relevant magnetic field information  $\mathbf{B}$  is not needed with the same precision as for SOL  $T_i$  measurements. A typical CX spectrum is not only composed of the active CX component but also has some additional contributions within the narrow bandpass filter range, and these are also encoded in the interferogram, contaminating the measurements. These are the passive and Bremsstrahlung radiation components. The origin and effects of these on the total CICERS signal, as well as approaches on how to deal with them, are addressed in the following section.

## III. BACKGROUND RADIATION

One of the main factors limiting the use of charge exchange radiation to infer relevant information about plasma parameters is the presence of additional background components besides the active CX contribution. For CICERS, those additional components are passive and Bremsstrahlung radiation. The passive contribution consists of the same characteristic photons as the active CX ones, generated by two main processes: Charge exchange with edge neutrals and electron impact excitation.<sup>10</sup> This type of radiation is typically generated toward the edge of the plasma, where ion temperatures are lower and the edge neutral concentration is higher. Passive radiation can be spread significantly along the lines of sight, especially those that graze the plasma edge. The visible Bremsstrahlung contribution is a spectral continuum radiation source.

Figure 1 shows a schematic of a typical total CX spectrum for the CVI emission line filtered by the narrow bandpass filter used for CICERS. These three different sources are encoded in the interference pattern. However, the FFT-demodulation treats it as a single source signal with parameters ( $I_{eff}$ ,  $\zeta_{eff}$ ,  $\Phi_{eff}$ ). It can be shown that the total signal  $S_{eff}$  is linear with respect to each individual spectral component,<sup>11</sup>

$$S_{eff} = S_{act} + S_{pas} + S_B, \quad (2)$$

where the subscript *act* refers to the active CX contribution, *pas* to passive, and *B* to Bremsstrahlung. Each of the components has the form  $S_i = \frac{I_i}{2} [1 + \zeta_i \cos \Phi_i]$ .

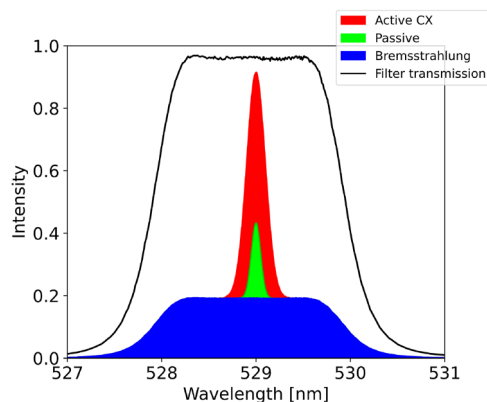


FIG. 1. Schematic of the total effective spectrum encoded in the CICERS signal. All the different radiation components are affected by the narrow bandpass filter transmission curve.

As the CX radiation only appears during NBI injection, a possible approach to isolate the active component is the interpolation of raw frames before and after the NBI injection. This approach can be used when diagnostic NBI blips are available.<sup>6</sup> However, it was found that non-linear changes in the background components were too significant during continuous NBI operation. This can be mitigated to some extent with an ad-hoc method, the ROI (Region Of Interest)-scaled interpolation,<sup>6</sup> but it remains unsatisfactory. The purpose of this work is to present a novel approach based on the modeling of background radiation that can be used to derive reliable experimental data when diagnostic blips are not available, i.e., when continuous NBI injection is used. The results presented in this section correspond to discharge No. 20230216.077, where continuous NBI was shot into an electron cyclotron resonance heating (ECRH) plasma during 2 s ( $t = 3\text{--}5$  s) with line-integrated densities  $\int n_e dl$  evolving from  $\sim 2$  to  $\sim 3$  m<sup>-2</sup>.

It can be shown from Eqs. (1) and (2) that the active CX contrast  $\zeta_{act}$  can be written in terms of the other interferogram parameters as

$$\zeta_{act} = \frac{\zeta_{eff} I_{eff} - \zeta_{pas} I_{pas}}{I_{eff} - (I_{pas} + I_B)}, \quad (3)$$

where the parameters and subscripts have the same meaning as previously introduced. Here, it was assumed that  $\Phi_{act} - \Phi_{pas} \sim 0$ . This assumption is justified by the reduced sensitivity of CICERS to flow velocity,<sup>6</sup> the small CVI flows at W7-X,<sup>12</sup> and the small central wavelength shift due to the Zeeman effect,<sup>13</sup> which makes the Doppler and multiplet phase shift terms<sup>6,14</sup> approximately equal for passive and active radiation sources, respectively. It has also been assumed that  $I_B \zeta_B / I_{act} \zeta_{act} \ll 1$ , which was further confirmed with simulations showing that  $\zeta_B \sim 0.0003$ . This approximation may not hold anymore at high  $n_e$  plasmas ( $n_e \sim 10^{20}$  m<sup>-3</sup>), where  $I_{act} \zeta_{act} \sim I_B \zeta_B$  as the Bremsstrahlung local emissivity scales as  $\varepsilon_B \propto n_e^2$ . The goal of the modeling approach is to model  $(I_B, I_{pas}, \zeta_{pas})$  so that the active CX contrast can be inferred via Eq. (3).

Since both Bremsstrahlung and passive radiation are not localized, the line-integration effects of each of the components need to be taken into account. For this reason, the pyFIDASim code<sup>15</sup> is used. The code generates a 3D grid and loads a local value of the normalized magnetic flux surface coordinate  $\rho$ , from a pre-computed equilibrium with the variational moments equilibrium code (VMEC),<sup>16,17</sup> in each individual cell. The code is able to extend the VMEC equilibrium to the SOL, up to  $\rho \sim 1.2$ . Once the view of CICERS is implemented in the code (see Sec. IV), it can compute the intersection between CICERS LOS and grid cells. The local Bremsstrahlung emissivity  $\varepsilon_B$  can be inferred using the electron density  $n_e$ , electron temperature  $T_e$ , and effective charge  $Z_{eff}$  profiles via the equation<sup>18</sup>

$$\frac{d\varepsilon_B}{d\lambda} = 7.57 \times 10^{-9} g \frac{n_e^2 Z_{eff}}{\lambda T_e} e^{hc/\lambda T_e}, \quad (4)$$

where  $\lambda$  is the wavelength in Å,  $n_e$  is the electron density in cm<sup>-3</sup>,  $Z_{eff}$  is the effective charge,  $T_e$  is the electron temperature in eV,  $\frac{d\varepsilon_B}{d\lambda}$  has units photons/(m<sup>-3</sup> Å s sr), and  $g$  is the Gaunt factor.<sup>19</sup>  $T_e$  and  $n_e$  profiles are taken from Thomson scattering,<sup>20</sup> while  $Z_{eff}$  is computed from  $n_e$  and carbon density profiles derived from CICERS (see Sec. V), assuming carbon as the predominant impurity.

An integral is performed both in wavelength, taking into account the narrow bandpass filter transmission curve (see Fig. 1 for reference), and along each individual CICERS LOS. An example of the resulting Bremsstrahlung intensity  $I_B$  overlaid on a computer aided design (CAD) vessel model of the CICERS view is shown in Fig. 2.

By comparing the modeled  $I_B$  with experimental measurements of background frames, it is found that modeling is able to predict the  $I_B$  contribution within an  $\sim 20\%$  accuracy. It is thought that such levels of uncertainty arise due to the quality of the profiles and neutral bremsstrahlung at the edge.

The direct modeling of passive radiation is a more complex process, as it relies on the precise knowledge of different parameters such as the edge neutral density and C<sup>6+</sup> and C<sup>5+</sup> densities, as well as the reaction rates for the different processes.<sup>10</sup> For this reason, a different approach is used. In W7-X, a dedicated spectrometer is able to routinely measure the passive CVI radiation intensity.<sup>21</sup> The method proposed here is to use the CVI intensity provided by the diagnostic to obtain a CVI emissivity profile, which is approximated to be a flux function. Although the flux-function approximation does not consider aspects such as the edge neutral asymmetries, the reconstruction of the CVI emissivity via CXRS data reported in Ref. 22 demonstrates the validity of this approximation. The CVI intensity  $I$  can be related to the emissivity  $\varepsilon$  as

$$I_i = W_i^\alpha \varepsilon_\alpha, \quad (5)$$

where  $W$  is the so-called diagnostic weight function and describes how sensitive each diagnostic LOS is to a portion of the phase space, which in this particular case is simply the normalized flux surface coordinate  $\rho$ .

Obtaining such emissivity constitutes an ill-posed inverse problem, which is solved in this case with the use of the zeroth Tikhonov regularization technique,<sup>23</sup> in which the following cost function is defined:

$$\mathcal{E}(\varepsilon|\alpha) = \|W\varepsilon - I\|_2^2 + \alpha \|I\|_2^2, \quad (6)$$

where  $\|\cdot\|_2$  denotes the  $L_2$  norm and  $\alpha$  is a hyper-parameter of the regression. The emissivity is finally obtained by minimization of the cost function, constraining  $\varepsilon$  to positive values to prevent non-physical solutions. Figure 3 shows (a) the CVI passive intensities as measured by the passive spectrometer as well as the reconstructed

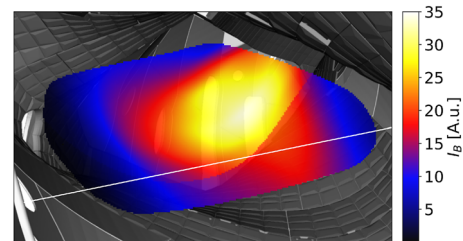


**FIG. 2.** Bremsstrahlung line-integrated intensity  $I_B$  for discharge No. 20230216.077,  $t = 4.462$  s. The intensity has been calibrated to CICERS intensity counts using the absolute intensity calibration presented in Sec. V. The white line represents the position in which the 2D  $T_e$  data (Fig. 6) were taken for the CICERS profile shown in Fig. 7.



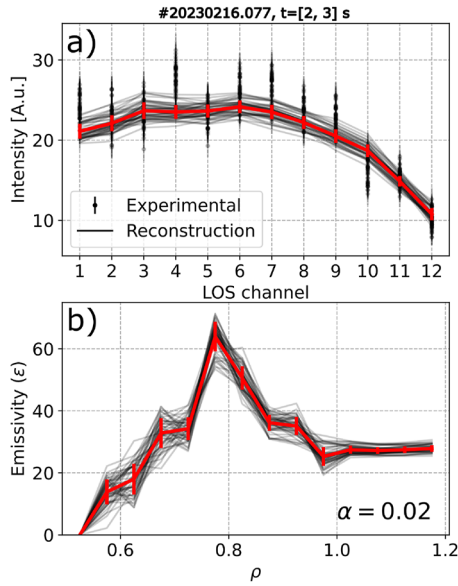


**FIG. 3.** (a) Intensity of the passive CVI radiation as measured by the passive spectrometer for each of the available LOS and (b) resulting emissivity  $\varepsilon(\rho)$  obtained after tomographic inversion. Results from each time stamp are plotted in black, while red lines represent the averaged ones. Red error bars represent the associated  $\pm\sigma$  standard deviation.

intensities with the emissivities shown in (b). The modeled passive intensity can then be inferred by performing the LOS integral of the emissivity along each individual LOS as

$$I_{pas}^{mod} = \int_{LOS} \varepsilon(\rho) dl. \quad (7)$$

The passive contrast can be approximated as the emissivity-weighted mean of the local contrast contribution,

$$\zeta_{pas} = \frac{\int_{LOS} \varepsilon(\rho) \zeta(T_i, \mathbf{B}) dl}{\int_{LOS} \varepsilon(\rho) dl}, \quad (8)$$

where

$$\zeta(T_i, \mathbf{B}) = \zeta_D(T_i) \zeta_M(\mathbf{B}). \quad (9)$$

$\zeta_D(T_i)$  is the Doppler contribution to the contrast term and depends mainly on the ion temperature  $T_i$  and  $\zeta_M(\mathbf{B})$  is the Zeeman contribution to the contrast, which depends on the magnetic field absolute value  $|\mathbf{B}|$  and on the angle between the magnetic field direction and the LOS direction  $\theta$ .<sup>6</sup> Each of these terms is computed locally in every individual grid cell and then averaged as shown in Eq. (8).

The reconstructed passive intensity as computed by Eq. (7) is arbitrarily calibrated to the emissivity counts resulting from the tomographic inversion, which depends on the hyper-parameter  $\alpha$  used for the inversion [see Eq. (6)]. A consistent cross-calibration to CICERS intensity counts can be carried out by comparing the simulated intensity to the experimental one obtained from background frames. The passive intensity can be decoupled from the Bremsstrahlung intensity for frames with no active CX contribution using

$$I_{pas}^{CICERS} = \frac{\zeta_{eff}}{\zeta_{pas}} I_{eff}. \quad (10)$$

Note that while  $\zeta_{pas}$  need to be previously evaluated as in Eq. (8), it does not require calibration as it only depends on the normalized distribution of  $\varepsilon(\rho)$ . A calibration factor can then be determined by direct comparison of  $\kappa_{cal} = I_{pas}^{CICERS} / I_{pas}^{mod}$ , which is then used to scale the modeled passive intensity during NBI injection.

The results of the modeled and cross-calibrated  $I_{pas}$  are shown in Figs. 4(a) and 4(b), respectively. The quantitative difference in shape between both figures comes from the defocusing of the imaging lens, which is not taken into account in the geometric calibration of the CICERS view and is probably due to the presence of edge neutral asymmetries not taken into account in the model. Therefore, the cross-calibration of  $I_{pas}$  with experimental CICERS frames is useful to alleviate the asymmetry effects previously mentioned.

Once  $(I_B, I_{pas}, \zeta_{pas})$  are known,  $\zeta_{act}$  is computed using Eq. (3), and finally,  $T_i$  can be derived using the diagnostic calibrations.<sup>6,24</sup> Since a  $T_i$  profile is needed to account for  $\zeta_{pas}$  [see Eq. (9)], a first computation of the 2D  $T_i$  map is carried out using the CICERS  $T_i$  profile from the previous time point, and the whole process is iterated until the resulting  $T_i$  profile derived from the  $T_i$  map in the nominal beam axis injection direction<sup>6</sup> converges. Convergence is typically found after  $\sim 3 - 4$  iterations. A schematic overview of the whole modeling process is shown in Fig. 5.

The resulting 2D  $T_i$  map is shown in Fig. 6(a), where the same  $T_i$  map obtained with the ROI-scaled method<sup>6</sup> is plotted for comparison in Fig. 6(b).  $T_i$  aligns much better with the overplotted

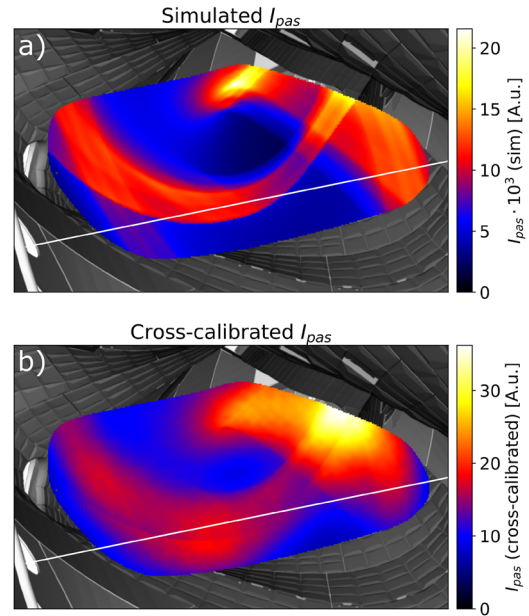


**FIG. 4.** (a) Modeled passive intensity and (b) same modeled intensity after cross-calibration with CICERS experimental passive intensity as obtained from frames with background radiation. The white line represents the position in which the 2D  $T_i$  data (Fig. 6) were taken for the CICERS profile shown in Fig. 7.

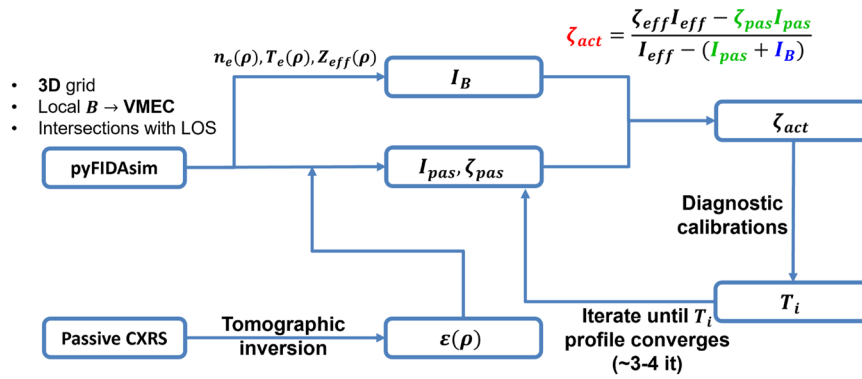


FIG. 5. Workflow overview used for the background modeling approach.

flux surfaces in the case of the modeling background subtraction, suggesting a better estimation of  $T_i$  by this method.

An additional validation of the  $T_i$  maps obtained by the background modeling method is shown in Fig. 7, where a CICERS  $T_i$  profile derived from the 2D  $T_i$  map shown in Fig. 6(a) is compared to the profile obtained by the toroidal view of the standard CXRS diagnostic at W7-X.<sup>8</sup> As shown, excellent agreement is found between both diagnostics up to the edge ( $\rho > 0.8$ ), where CICERS predicts slightly higher temperatures. This effect was also observed using the ROI-scaled method,<sup>6</sup> and while the reason is not clear yet, a possible explanation may be due to an imprecise determination of the background radiation toward the edges of the plasma. Since the active CX radiation intensity is reduced in this region, it is more

sensitive to uncertainties in the modeled parameters, such as, e.g., the uncertainty in the Bremsstrahlung intensity  $I_B$ .

As mentioned earlier, the uncertainty on  $I_B$  was assessed to be  $\Delta I_B \sim 20\%$ . This level of uncertainty renders the method introduced here only useful for low- $n_e$  plasmas (up to  $\int n_e dl \sim 6-7 \text{ m}^{-2}$ ), since for high- $n_e$ , the errors on the Bremsstrahlung contribution are comparable to the active CX signal as  $\epsilon_B \propto n_e^2$  [see Eq. (4)]. As of now, the only method to infer reliable measurements with CICERS at high- $n_e$  plasmas is to interpolate the background radiation during NBI blips.

#### IV. PYFIDASIM IMPLEMENTATION

The view of CICERS was implemented in the pyFIDASIM code and was reliably used for the modeling background subtraction

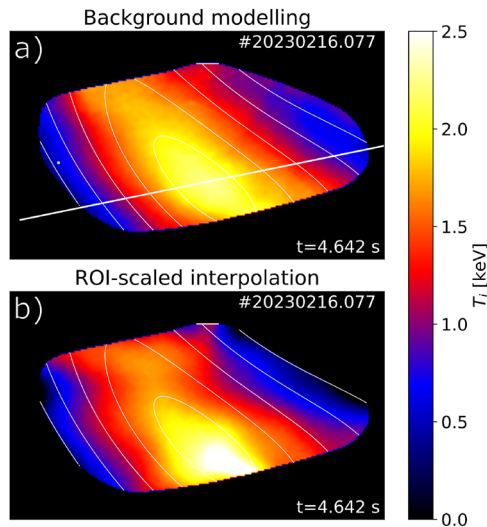


FIG. 6. (a) 2D  $T_i$  map obtained from the modeling background subtraction method, and (b) same 2D  $T_i$  map obtained with the ROI-scaled background subtraction.<sup>6</sup> Note how the adjustment of  $T_i$  to the overplotted flux surface contours is much better for the background modeling case. The white line in (a) represents the position in which the data were taken for the CICERS profile shown in Fig. 7.

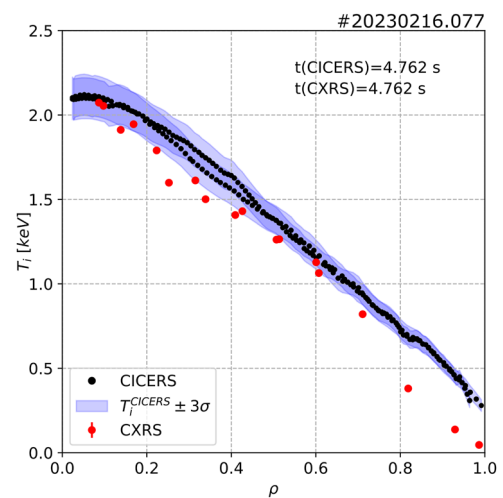


FIG. 7. Ion temperature profile obtained from the 2D map shown in Fig. 6(a) and comparison with the CXRS toroidal view (port AEA21) profile. The blue area corresponds to the  $\pm 3\sigma$  confidence interval accounting for CICERS systematic errors. CICERS  $T_i$  data are taken in the positions along the white line shown in Figs. 2, 4, and 6. The two CICERS profiles correspond to inboard/outboard data.

method introduced in the previous section. However, the main purpose of the code is to model the NBI injected neutrals. It implements a Monte Carlo approach and uses a collisional-radiative model to predict the neutral density for each energy component ( $E/1$ ,  $E/2$ ,  $E/3$ , Halo) and different main quantum numbers ( $n = 1, 2$ ). The code has already been tested and validated in W7-X for impurity density measurements from standard CXRS<sup>9</sup> and fast-ion  $H_\alpha$  emission characterization.<sup>25</sup>

The intensity of the CVI CX radiation can be modeled via

$$I_{act} = \frac{1}{4\pi} \int_{LOS} n_{C6+} \sum_{E,i} n_H^{E,i} \langle \sigma v \rangle_{E,i}^{CX} dl, \quad (11)$$

where  $n_{C6+}$  is the density of the  $C^{6+}$  species,  $n_H^{E,i}$  is the density of the NBI injected neutrals, and  $\langle \sigma v \rangle_{E,i}^{CX}$  represents the reaction rate of the CX cross section. The subscript  $E$  refers to the different energy components  $E = [E/1, E/2, E/3, Halo]$  and  $i$  to the main quantum numbers  $i = [1, 2]$ . Figure 8 shows a comparison of the modeled and experimental  $I_{act}$  contours. Here, a set of precomputed reaction rates compiled for the ASDEX Upgrade tokamak<sup>9,26</sup> is used. The impurity density profile used for the simulations is the one derived and shown in Sec. V.

Figure 8(a) plots the results of the simulation using the nominal NBI S4 parameters, where an offset between the simulation and experimental contours is observed. A good agreement is found between modeled and experimental contours when a 4.6 cm upward shift is introduced in the NBI source position, as shown in Fig. 8(b). A discrepancy can be observed on the right side of the innermost contours, which is related to imprecisions in the neutral modeling carried out by pyFIDASim. The shift in the source position is thought to be due to the effects of the W7-X magnetic fields on the

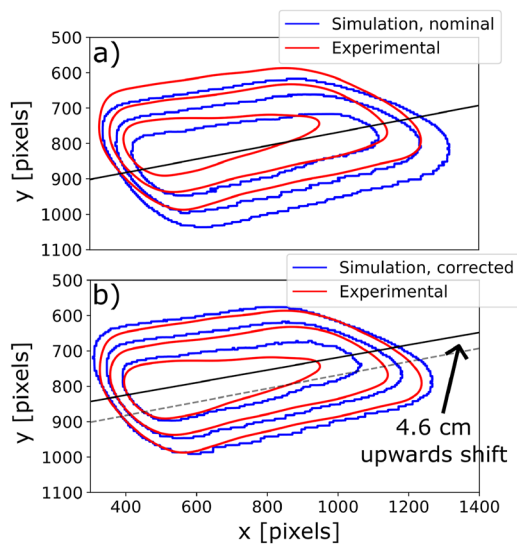


**FIG. 8.** Contours of the experimental (red) and simulated (blue) CICERS  $I_{act}$  using (a) nominal beam parameters and (b) introducing a 4.6 cm upward shift in the beam source position.

NBI, as reported by NBI calorimeter loads.<sup>27</sup> A  $\sim 5$  cm upward shift has been previously reported by Bayesian BES modeling for sources S7 and S8 in W7-X.<sup>28</sup>

### A. Spatial localization of the active CX radiation

The NBI injected neutrals provided by the pyFIDASim code can be further used to assess how well the active CX radiation is localized in the plasma and, thus, to investigate line-integration effects. The typical approach to localize the CX radiation is the closest approach (CA) method, where the radiation is assumed to originate at the point of closest approach along each individual LOS to the beam axis. An alternate approach based on evaluating the center of mass (COM) of the active CX radiation can be used.<sup>9</sup> Here, the spatial location of each individual LOS is evaluated by performing the following LOS integral:

$$s_{COM} = \frac{\int_{LOS} s w dl}{\int_{LOS} w dl}, \quad (12)$$

where  $s = \rho^2$  and  $w$  are the weights of the emissions along the LOS computed as

$$w = \sum_{E,i} n_H^{E,i} \langle \sigma v \rangle_{E,i}^{CX}. \quad (13)$$

The difference between the spatial location as obtained both by CA and COM is shown in Fig. 9. While some spatial variations can be observed due to the complex 3D geometry of W7-X, the differences found are of the order of  $\sim 1\%$ – $3\%$  overall. This is consistent with previous similar studies carried out for the W7-X standard CXRS.<sup>9</sup>

The weights computed can be further used for the assessment of the spread of active CX radiation along the LOS for the whole 2D map. The full width at half maximum (FWHM) of the distribution of  $w$  is shown in Fig. 10. It can be seen that values toward the edge of the plasma have a higher FWHM (and, thus, line-integration effects), while those closer to the core of the plasma are smaller, showing a reduction in the line-integration effects in this region. In addition, these line-integration effects are different on the inboard (right) and outboard (left) sides of the plasma.

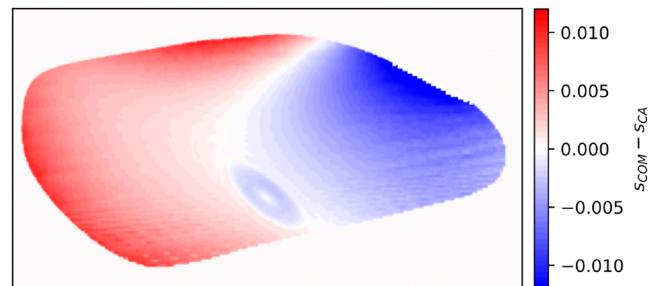


**FIG. 9.** Difference between the closest approach (CA) and center of mass (COM) methods. Both methods provide a consistent evaluation of the origin of the CX radiation, with negligible differences ( $\sim 1\%$ – $3\%$ ) throughout the CICERS typical 2D map.

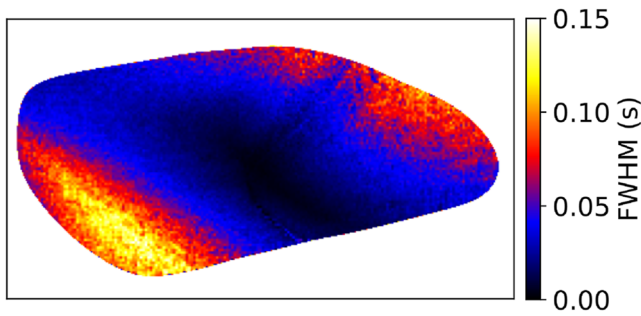


**FIG. 10.** Full Width at Half Maximum (FWHM) of weights [computed as Eq. (13)] along each LOS.

## V. IMPURITY DENSITIES

The impurity density can be related to the intensity of the CX radiation as<sup>36</sup>

$$n_{C6+} = 4\pi \frac{I_{act}}{\sum_{E,i} \int_{LOS} n_H^{E,i} \langle \sigma v \rangle_{E,i}^{CX} dl}, \quad (14)$$

where all the parameters have the same meaning as in Eq. (11). To derive carbon impurity density  $n_C$  maps from the diagnostic signal, an absolute calibration of the CICERS signal has been performed by using an absolutely calibrated Ulbricht sphere. The sphere was placed in front of the fiber bundle that collects light for the CICERS and SOL CIS diagnostics in the laboratory. The resulting absolute calibration has been additionally corrected by the calibrated transmission factors of the window and mirror components of the immersion tube used to recollect light from the plasma and redirect it to the fiber bundle. The results of the impurity density map obtained after absolute calibration are shown in Fig. 11, overlaid with flux-surface contours. Again, a good adjustment of  $n_C$  to the contours is found. While overall smooth, a fringe-like behavior is observed in the bottom center part of the map. It is believed to be due to line-integration effects and the finite size grid used for the simulations ( $dR, dZ = 1$  cm). A slight increase in  $n_C$  can be observed as a white spot between  $\rho = 0.6$  and  $\rho = 0.4$  on the outboard (left

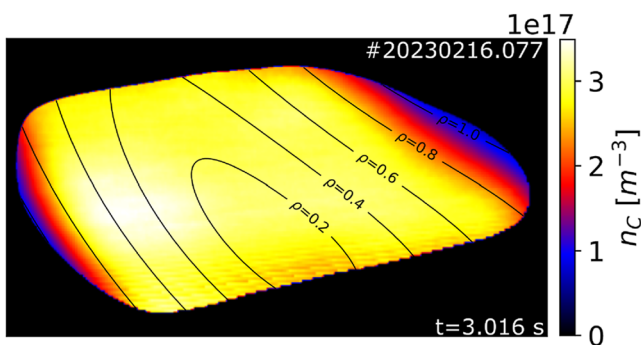


**FIG. 11.** 2D  $n_C$  map obtained from the CICERS experimental signal and pyFIDASim neutral beam simulations.

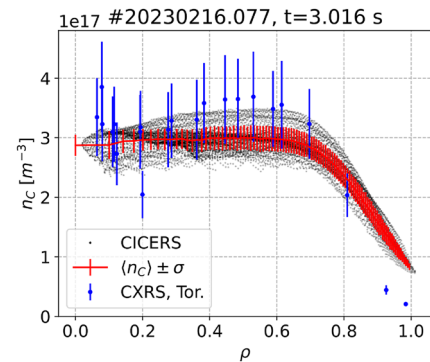


**FIG. 12.** CICERS  $n_C$  profile (red line) derived from the flux-surface average of the CICERS data points (black dots) and CXRS  $n_C$  data. CICERS errors correspond to the  $\pm 1\sigma$  standard deviation resulting from flux-surface averaging.

side of the map. While not clear, this increase in  $n_C$  is thought to be due to an underestimation/overestimation of the injected neutrals modeled by pyFIDASim, as already reported in Refs. 9 and 25. This effect is also the reason for the discrepancies in the contours in Fig. 8. The flux-surface asymmetries are assessed and found to be on the order of  $n_C / \langle n_C \rangle \sim 10\%$ , which are higher than the neoclassical predictions for  $C^{6+}$ .<sup>29</sup> This topic will be further investigated in the upcoming W7-X experimental campaign.

Figure 12 plots a 1D profile showing all the CICERS  $n_C$  data-points in black. The red profile corresponds to the flux-surface averaged values, with error bars corresponding to the  $\pm 1\sigma$  standard deviation evaluated in the flux-surface averaging. The nominal NBI power (1.8 MW) is downscaled by a factor of 0.6 to match the CXRS  $n_C$  profile. This factor accounts for beam scrapping by the NBI port and beam attenuation in the SOL.<sup>9</sup> A similar factor was used for standard CXRS<sup>9</sup> (0.7), and the need for a smaller factor is thought to be due to the introduction of the shift in source position. While still unclear, an additional possible reason for the discrepancy might be the quality of the absolute calibration. This point will be further addressed in future work by performing a similar analysis with BES-modeling-inferred NBI injected neutrals.<sup>28</sup>

In general, good agreement is found between CXRS and CICERS data, as well as for  $n_C$ . Again, a systematic overestimation of  $n_C$  is predicted by CICERS toward the edge, as observed in the  $T_i$  profiles (see Fig. 7), reaffirming the hypothesis of an underestimation of background contribution toward the edge of the plasma.

## VI. CONCLUSIONS

CICERS is a powerful diagnostic from which 2D maps of relevant plasma parameters can be obtained with enhanced spatial resolution by the analysis of the active CX radiation. In this work, a novel approach to overcome the diagnostic limitations in terms of subtracting the background radiation components during continuous NBI injection to derive reliable  $T_i$  measurements is presented. For this purpose, the different contributions to the active contrast  $\zeta_{act}$  as shown in Eq. (3) are modeled: the Bremsstrahlung line-integrated intensity  $I_B$  is assessed via an analytic expression



depending on  $n_e$ ,  $T_e$ , and  $Z_{eff}$ , and the passive intensity  $I_{pas}$  and passive contrast  $\zeta_{pas}$  are determined via a tomographic inversion on the passive intensity measured by a dedicated spectrometer. The method is shown to provide excellent results for  $T_i$  measurements with continuous NBI injection in low- $n_e$  plasmas up to the edge ( $\rho > 0.8$ ), but the errors on the Bremsstrahlung contribution ( $\Delta I_B \sim 20\%$ ) limit its use for high- $n_e$  plasmas as  $\varepsilon_B \propto n_e^2$ . As of now, the best approach for reliable measurements at high  $n_e$  is the use of diagnostic NBI blips. Finally, CICERS was successfully implemented in the pyFIDAsim code. The modeled NBI neutrals, along with an absolute calibration, were exploited to reconstruct, for the first time, a 2D  $n_C$  map. These results were validated against standard CXRS, and good agreement was found.

## ACKNOWLEDGMENTS

R.L.-C. and E.V. gratefully acknowledge the financial support of the European Research Council (ERC) under the European Union's Horizon 2020 research innovation program (Grant Agreement No. 805162) and the Ministerio de Ciencia e Innovación under the PID program (Grant Agreement No. PID2020-116822RB-I00). This work has partially been carried out within the framework of the EUROfusion Consortium, funded by the European Union via the Euratom Research and Training Program (Grant Agreement No. 101052200-EUROfusion). The views and opinions expressed are, however, those of the author(s) only and do not necessarily reflect those of the European Union or the European Commission. Neither the European Union nor the European Commission can be held responsible for them.

## AUTHOR DECLARATIONS

### Conflict of Interest

The authors have no conflicts to disclose.

## Author Contributions

**R. Lopez-Cansino:** Conceptualization (equal); Data curation (equal); Formal analysis (equal); Investigation (equal); Methodology (equal); Software (equal); Validation (equal); Visualization (equal); Writing – original draft (equal). **V. Perseo:** Methodology (equal); Resources (equal); Supervision (equal); Validation (equal); Writing – review & editing (equal). **E. Viezzer:** Funding acquisition (equal); Methodology (equal); Resources (equal); Supervision (equal); Validation (equal); Writing – review & editing (equal). **O. P. Ford:** Data curation (equal); Resources (equal); Supervision (equal); Writing – review & editing (equal). **M. Kriete:** Investigation (equal); Methodology (equal). **T. Romba:** Data curation (equal); Software (equal); Validation (equal). **J. Rueda-Rueda:** Methodology (equal); Software (equal). **P. Z. Poloskei:** Data curation (equal); Software (equal). **F. Reimold:** Supervision (equal); Writing – review & editing (equal).

## DATA AVAILABILITY

The data that support the findings of this study are available from the corresponding author upon reasonable request.

## REFERENCES

- <sup>1</sup>V. Perseo, D. Gradic, R. König, O. P. Ford, C. Killer, O. Grulke, D. A. Ennis *et al.*, “Coherence imaging spectroscopy at Wendelstein 7-X for impurity flow measurements,” *Rev. Sci. Instrum.* **91**, 013501 (2020).
- <sup>2</sup>J. Howard, “Coherence imaging spectro-polarimetry for magnetic fusion diagnostics,” *J. Phys. B: At., Mol. Opt. Phys.* **43**, 144010 (2010).
- <sup>3</sup>D. Gradic, “Doppler coherence imaging of ion dynamics in the plasma experiments VINETA.II and ASDEX Upgrade,” Ph.D. thesis, Technischen Universität Berlin, 2018.
- <sup>4</sup>D. Gradic, V. Perseo, D. Kriete, M. Krychowiak, R. König, Y. Feng, M. Otte, T. S. Pedersen, Y. Gao, M. Jakubowski *et al.*, “2D coherence imaging measurements of  $C^{2+}$  ion temperatures in the divertor of Wendelstein 7-X,” *Nucl. Fusion* **61**, 106041 (2021).
- <sup>5</sup>D. Kriete, V. Perseo, D. Gradic, D. Ennis, R. König, D. Maurer *et al.*, “Ion temperature imaging in the divertor of the W7-X stellarator using coherence imaging spectroscopy,” in 25th Topical Conference on High Temperature Plasma Diagnostics (HTPD 2024), 2024.
- <sup>6</sup>R. Lopez-Cansino, V. Perseo, E. Viezzer, D. M. Kriete, O. Ford, T. Romba, and P. Z. Poloskei, “First measurements with a coherence imaging charge exchange recombination spectroscopy (CICERS) diagnostic at Wendelstein 7-X,” *Plasma Phys. Controlled Fusion* **66**, 045012 (2024).
- <sup>7</sup>N. Chaudhary, M. Hirsch, T. Andreeva, J. Geiger, U. Hoefel, K. Rahbarnia, G. A. Wurden, and R. Wolf, “Radial localization of electron temperature pedestal and ELM-like events using ECE measurements at Wendelstein 7-X,” *EPJ Web Conf.* **277**, 03004 (2023).
- <sup>8</sup>O. Ford, L. Vanó, J. Alonso, J. Baldzuhn, M. Beurskens, C. Biedermann, S. Bozhrenkov, G. Fuchert, B. Geiger, D. Hartmann *et al.*, “Charge exchange recombination spectroscopy at Wendelstein 7-X,” *Rev. Sci. Instrum.* **91**, 023507 (2020).
- <sup>9</sup>T. Romba, F. Reimold, R. Jaspers, A. Edmondson, O. Ford, B. Geiger, S. Jabłoński, M. Kubkowska, T. Neelis, P. Z. Poloskei *et al.*, “Evaluation and validation of radial impurity density profiles from CXRS using neutral beam modelling in W7-X,” *Plasma Phys. Controlled Fusion* **65**, 075011 (2023).
- <sup>10</sup>E. Viezzer, T. Pütterich, R. Dux, A. Kallenbach, A. U. Team *et al.*, “Investigation of passive edge emission in charge exchange spectra at the ASDEX Upgrade tokamak,” *Plasma Phys. Controlled Fusion* **53**, 035002 (2011).
- <sup>11</sup>J. Howard, R. Jaspers, O. Lischtschenko, E. Delabie, and J. Chung, “Imaging charge exchange recombination spectroscopy on the TEXTOR tokamak,” *Plasma Phys. Controlled Fusion* **52**, 125002 (2010).
- <sup>12</sup>J. Alonso, O. Ford, L. Vanó, S. Äkäslompolo, S. Buller, R. McDermott, H. Smith, J. Baldzuhn, C. Beidler, M. Beurskens, S. Bozhrenkov, K. Brunner, I. Calvo, D. Carralero, A. Dinklage, T. Estrada, G. Fuchert, J. Geiger, J. Knauer, A. Langenberg, N. Pablant, E. Pasch, P. Poloskei, J. Velasco, T. Windisch, and T. W.-X. Team, “Plasma flow measurements based on charge exchange recombination spectroscopy in the Wendelstein 7-X stellarator,” *Nucl. Fusion* **62**, 106005 (2022).
- <sup>13</sup>A. Blom and C. Jupén, “Parametrization of the Zeeman effect for hydrogen-like spectra in high-temperature plasmas,” *Plasma Phys. Controlled Fusion* **44**, 1229 (2002).
- <sup>14</sup>S. Silburn, “A Doppler coherence imaging diagnostic for the mega-amp spherical tokamak,” Ph.D. thesis, Durham University, 2014.
- <sup>15</sup>C. Swee, B. Geiger, R. Dux, S. Kumar, J. Castillo, A. Bader, and M. Gerard, “Impurity transport studies at the HSX stellarator using active and passive CVI spectroscopy,” *Plasma Phys. Controlled Fusion* **64**, 015008 (2021).
- <sup>16</sup>S. P. Hirshman and J. C. Whitson, “Steepest descent moment method for three-dimensional magnetohydrodynamic equilibria,” *Phys. Fluids* **26**, 3553 (1983).
- <sup>17</sup>M. Grahrl, J. Svensson, A. Werner, T. Andreeva, S. Bozhrenkov, M. Drevlak, J. Geiger, M. Krychowiak, and Y. Turkin, “Web services for 3D MHD equilibrium data at Wendelstein 7-X,” *IEEE Trans. Plasma Sci.* **46**, 1114–1119 (2018).
- <sup>18</sup>M. Van Zeeland, J. Yu, W. Heidbrink, N. Brooks, K. Burrell, M. Chu, A. Hyatt, C. Muscatello, R. Nazikian, N. Pablant *et al.*, “Imaging key aspects of fast ion physics in the DIII-D tokamak,” *Nucl. Fusion* **50**, 084002 (2010).
- <sup>19</sup>P. Van Hoof, R. Williams, K. Volk, M. Chatzikos, G. J. Ferland, M. Lykins, R. Porter, and Y. Wang, “Accurate determination of the free-free Gaunt



factor—I. Non-relativistic Gaunt factors,” *Mon. Not. R. Astron. Soc.* **444**, 420–428 (2014).

<sup>20</sup>E. Pasch, M. Beurskens, S. A. Bozhenkov, G. Fuchert, J. Knauer, R. C. Wolf *et al.*, “The Thomson scattering system at Wendelstein 7-X,” *Rev. Sci. Instrum.* **87**, 11E729 (2016).

<sup>21</sup>O. P. Ford, A. Langenberg, T. Romba, P. Pölöskei, M. Zanini, S. Bannmann, T. Gonda, K. Ida, R. Lopez Cansino *et al.*, “Visible core spectroscopy at W7-X,” *Rev. Sci. Instrum.* (in press) (2024).

<sup>22</sup>L. Vano, “Carbon content and transport investigations on Wendelstein 7-X with charge exchange recombination spectroscopy,” Ph.D. thesis, Technischen Universität Berlin, 2022.

<sup>23</sup>J. Rueda-Rueda, M. Garcia-Munoz, E. Viezzer, P. A. Schneider, P. Oyola, J. Galdon-Quiroga, M. Salewski, B. S. Schmidt, J. Garcia-Dominguez, and A. Upgrade team, “Tomographic reconstructions of the fast-ion phase space using imaging neutral particle analyser measurements,” *Plasma Phys. Controlled Fusion* **66**, 065025 (2024).

<sup>24</sup>V. Perseo, R. Lopez-Cansino, D. Kriete, S. Akhundzada, O. Ford, D. Gradic, F. Reimold, D. Ennis, E. Viezzer *et al.*, “Validation of delay dispersion extrapolation for coherence imaging spectroscopy,” in 25th Topical Conference on High Temperature Plasma Diagnostics (HTPD 2024), 2024.

<sup>25</sup>P. Z. Poloskei, B. Geiger, A. Jansen van Vuuren, S. Äkäslompolo, O. Ford, A. Spanier, T. Neelis, P. McNeely, D. Hartmann *et al.*, “Experimental characterization of the active and passive fast-ion H-alpha emission in W7-X using FIDASIM,” *Nucl. Fusion* **64**, 026008 (2023).

<sup>26</sup>R. McDermott, R. Dux, T. Pütterich, B. Geiger, A. Kappatou, A. Lebschy, C. Bruhn, M. Cavedon, A. Frank, N. d. Harder, and E. Viezzer, “Evaluation of impurity densities from charge exchange recombination spectroscopy measurements at ASDEX Upgrade,” *Plasma Phys. Controlled Fusion* **60**, 095007 (2018).

<sup>27</sup>S. Lazerson, P. McNeely, N. Rust, O. Ford, M. Beurskens, D. Kulla, D. Hartmann, R. Wolf *et al.*, “Neutral beam experiments with upgraded power on Wendelstein 7-X,” in 29th IAEA Fusion Energy Conference (FEC 2023), 2023.

<sup>28</sup>S. Bannmann, O. Ford, U. Hoefel, P. Poloskei, A. Pavone, S. Kwak, J. Svensson, S. Lazerson, P. McNeely, N. Rust *et al.*, “Fast forward modeling of neutral beam injection and halo formation including full Balmer- $\alpha$  emission prediction at W7-X,” *J. Instrum.* **18**, P10029 (2023).

<sup>29</sup>A. Alonso, O. Ford, C. Brandt, D. Carralero, A. Dinklage, J. Garcia-Regana, A. Langenberg, A. Mollen *et al.*, “Understanding ion and impurity flows in the Wendelstein 7-X stellarator,” in 46th EPS Conference on Plasma Physics, 2019.